Onset voltage of a particle-initiated negative corona in a co-axial cylindrical configuration

M M El Bahy[1], S A Ward[2], R Morsi[2] and M Badawi[2]

[1] Faculty of Engineering (at Benha), Benha University, Cairo, Egypt
[2] Faculty of Engineering (at Shoubra), Benha University, Cairo, Egypt

E-mail: moh23_bad@yahoo.com

Abstract

This paper presents a theoretical and experimental study of the effect of conducting particles on the onset voltage of a negative corona in air-insulated co-axial cylindrical configurations. The conducting particles are spheres or wires of varying dimensions. The particle is fixed either on the inner or the outer cylinder. The calculated onset voltage of the negative corona is based on the criterion developed for the formation of repetitive negative coronas, Trichel pulses. This calls first for an accurate calculation of the electric field in the vicinity of the particle where avalanches grow. The investigated gap in the presence of a particle is a three-dimensional field problem due to the asymmetrical position of the particle inside the gap. The three-dimensional electric field is calculated using the charge simulation technique with a new charge distribution. An experimental set-up is built up to measure the onset voltage of a negative corona initiated by particles in an air-insulated co-axial configuration to check the accuracy of the present calculation. The effect of varying field nonuniformity, particle shape, size and position on the onset voltage of the negative corona is investigated. The calculated onset voltage values agree well with those measured experimentally.

(Some figures may appear in colour only in the online journal)

1. Introduction

The use of gas-insulated systems (GISs) in the power system network has acquired considerable importance because of its compactness, maintenance-free, safe and reliable operation. The reliability of GIS is adversely affected by the presence of contaminating conducting particles in the insulation structure. These particles initiate partial discharges forming electrons and ions in the medium, and then initiating the process of breakdown, which leads to a catastrophic failure of the insulation structure [1–6]. These particles drastically reduce the onset voltages of the corona and breakdown [2, 4, 6–8]. Insulating particles are not so harmful as they have little effect on the insulating properties of gases; however, 20% of failures in GIS are due to the existence of contaminating conducting particles [9, 10]. These particles may have any shape or size. It may be spherical or filamentary (like wire) or in the form of fine dust. Wire particles are more harmful and their effects

are more pronounced at higher gas pressures. The field at the particle tip exceeds the limiting dielectric strength of the gas, at least locally, initiating a corona discharge, which in time develops into a breakdown. The particles may be free to move under the influence of the applied field or may be fixed on the electrodes in the form of a protrusion representing surface roughness. When they are present and are in contact with one of the electrodes, they acquire a charge, depending on the applied field and their size. At a particular field they will be lifted and move towards the inner cylinder when set free on the outer cylinder. Before reaching the lifting field, the field at the particle may be sufficient to initiate a corona discharge.

In this paper, theoretical and experimental determination of the effect of a conducting particle on the onset voltage of a negative corona in the air-insulated co-axial configuration is presented. This configuration has been used for simulating the structure of GIS. The onset voltage of a negative corona is studied since it is somewhat lower than the onset values of
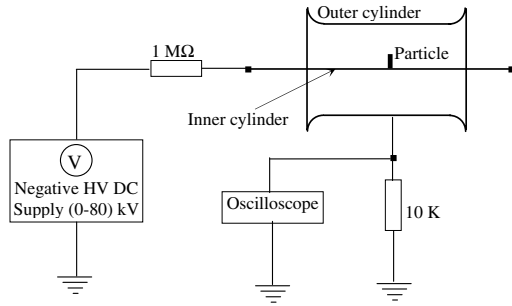
J. Phys. D: Appl. Phys. **46** (2013) 045205

M M El Bahy *et al*

Figure 1. Schematic diagram of the experimental set-up.

a positive corona [11]. Determination of the onset voltage of a negative corona is based on the criterion developed for the formation of repetitive negative coronas, Trichel pulses [12], which require an accurate calculation of the electric field in the vicinity of the particle. The presence of particles in a co-axial cylinder results in a three-dimensional field problem with an asymmetrical field about the particle surface, due to the asymmetrical position of the particle inside the gap and the asymmetrical influence of the co-axial cylinder on the particle surface electric field. The three-dimensional electric field is calculated using the charge simulation technique (CST) [6, 7, 12–14] with a new charge distribution. To the best of our knowledge, the calculation of three-dimensional electric field in co-axial cylinders in the presence of particles has not yet been reported in the literature. The conducting particles are spheres or wires of varying dimensions, fixed either on the inner or the outer cylinder. The wire particle is a cylinder hemispherically terminated at both ends positioned to touch radially either the inner or the outer cylinder. The calculated field values agree well with those values obtained theoretically before [5]. Then, the field values are used for calculating the onset voltage of the negative corona. The calculated onset voltage values agree satisfactorily with the values measured experimentally.

2. Experimental set-up

The experimental set-up is schematically illustrated in figure 1; this set-up has been built up to measure the onset voltage of a particle-initiated negative corona in an air-insulated co-axial cylinder. The experimental work was carried out inside the laboratory in dry air at room temperature (22–25 °C) and atmospheric pressure using a co-axial cylindrical configuration made of brass. The co-axial configurations had an inner cylinder of varying radii (5.5, 6, 8 and 11 mm) and an outer cylinder of constant radius (41 mm). The length of the inner cylinder is 800 mm supported at both ends by insulating supports and is extended along the axis of the 200 mm long outer cylinder. The outer cylinder edge is smoothed and rounded to avoid flashover or an early discharge, figure 1.

Spherical and wire particles of different dimensions were used in the experiment and each particle was fixed either on the inner or the outer cylinder. Stainless steel spherical particles of radii 0.5, 0.75, 1, 1.25, 1.5 and 2 mm were used. Also, tin wire particles of radii 0.25, 0.375 and 0.5 mm with varying lengths in the range 2–20 mm were used.
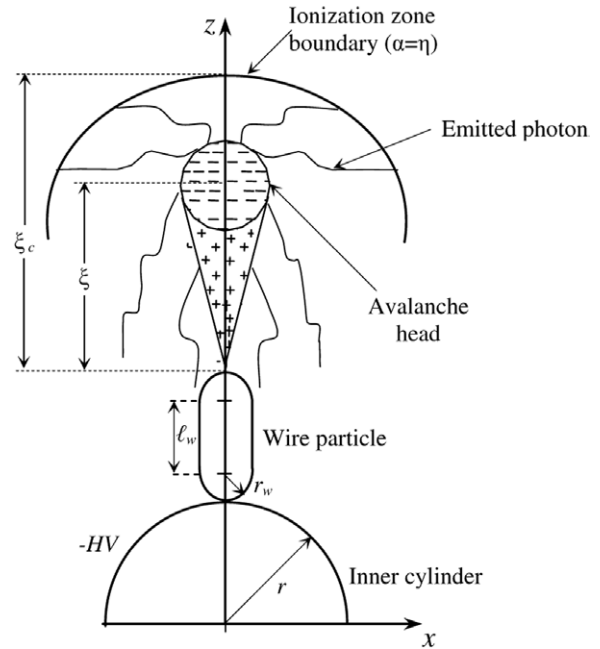

Figure 2. Growth of primary avalanche, in a negative corona, along the gap axis in the vicinity of a wire particle fixed at the inner cylinder.

A high-voltage dc source with negative polarity and output voltage up to 80 kV (Hipotronics, Model 880PL-10 mA) was used to energize the stressed cylinder. The high-voltage source has a voltage metering device, for measuring the output applied voltage, with full scale accuracy of ±2%. The stressed cylinder was connected to the HV source through a water resistance of 1 MΩ as a current-limiting resistor, to prevent any damage of instruments if flashover occurred, and the other cylinder was grounded through a 10 kΩ resistor. A digital storage oscilloscope (Gwinstek, Model GDS-1052-U) was connected across the 10 kΩ resistor to detect and monitor the corona pulse.

To determine the onset voltage of the negative corona the applied voltage was raised to about 90% of the expected value at a rate of 1 kV s^{-1} and thereafter at a rate of 0.1 kV s^{-1} until the initiation of the corona pulse (Trichel pulse) on the oscilloscope takes place [12]; the applied voltage is the corona onset value. At least 10 measurements were taken for each measuring point to estimate the mean value, and the relative standard deviation of the mean values was generally smaller than 0.44% for all measuring points. The time interval between two measurements was in the range 1–2 min, and during this time interval the stressed cylinder was grounded to leak its surface charge; in addition, a weak air flow was used to clean the air gap from space charge initiated by the corona.

3. Method of analysis

3.1. Onset voltage of the negative corona

When the electric field at the particle tip reaches the threshold value for ionization of gas molecules by electron collision, an electron avalanche starts to develop along the direction away from the particle, figure 2. The growth of the avalanche

continues as long as Townsend's first ionization coefficient, $\alpha(\xi)$, is greater than the electron attachment coefficient, $\eta(\xi)$, and terminates at $\xi = \xi_c$; i.e. at the ionization-zone boundary [7, 15], where the electrons get attached to the gas molecules and form negative ions. With the avalanche growth, more electrons are developed at its head, more photons are emitted in all directions, and more ions that are positive are left in the avalanche's wake. The electric field is a result of the field due to the applied voltage and the space charge field of the primary avalanche itself [16].

For a successor avalanche to be started, the preceding avalanche should somehow provide an initiating electron at the particle tip, possibly by photoemission, positive ion impact, metastable action or field emission. Only the first mechanism (electron emission from the cathode by photons) is considered in the mathematical formulation of the onset criterion, where at least one photoelectron ($N_{eph} = 1$) is emitted by the photons of the primary avalanche to keep the discharge self-sustaining [7, 15],

i.e. $N_{eph} = \gamma_{ph} \int_0^{\xi_c} \alpha(\xi) g(\xi) \exp\left[\int_0^{\xi_c} (\alpha(\xi) - \eta(\xi)) \, d\xi\right]$
$\times \exp(-\mu\xi) \, d\xi,$ (1)

where γ_{ph} is Townsend's second coefficient due to the action of photons, μ is the absorption coefficient in air, ξ_c is the distance measured from the particle tip determining the ionization-zone boundary and $g(\xi)$ is a geometric factor to account for the fact that some photons are not received by the cathode, appendix A. The condition for a new (successor) avalanche to be developed is

$$N_{eph} \geqslant 1.$$ (2)

The onset voltage of the corona does not appear explicitly in the relation (1). However, the values of $\alpha(\xi)$ and $\eta(\xi)$, which are given in [17], are affected by the electric field produced due to the negative applied voltage $(-V)$. The discharge parameters $\alpha(\xi)$, $\eta(\xi)$, γ_{ph} and μ are given in appendix B. The onset voltage is the critical value, which fulfils equality (2).

3.2. Electric field calculation on and around the particle surface

The analysis is based on CST in which the charge on the surfaces of the particle and the inner cylinder is replaced by a set of fictitious simulation charges arranged inside each of them, wheras the surface charge on the outer cylinder is replaced by another set of charges arranged outside its surface. The satisfaction of the pertinent boundary conditions results in a set of equations whose simultaneous solution determines the unknown simulation charges. Knowing the simulating charges, the electric potential and field can be calculated at any point on and around the particle surface in the investigated gap [6, 12–14].

3.2.1. Simulation technique.
The analysis is based on CST [6, 12–14] in which the distributed charge on each surface of the inner and outer cylinders is replaced by a set of n discrete line charges of varying longitudinal charge density arranged axially inside and outside their surfaces, respectively, figure 3.
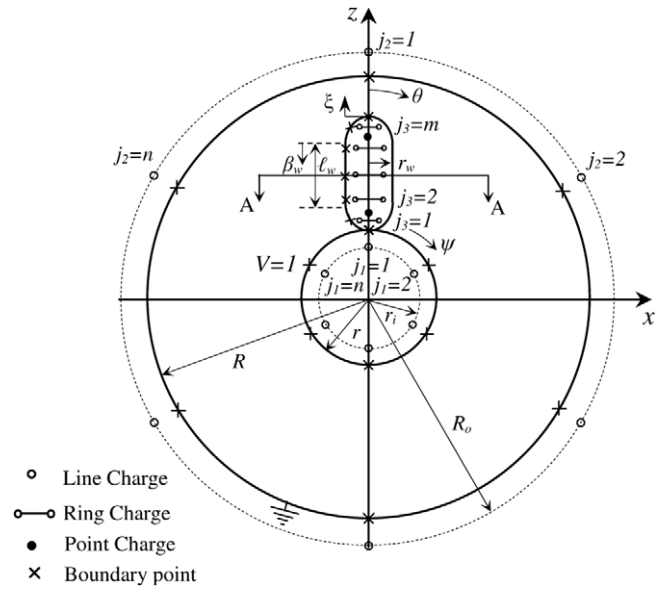

Figure 3. Discrete simulation charges and boundary points in a cross section of co-axial cylinder gap with a wire particle placed in contact with the inner cylinder.
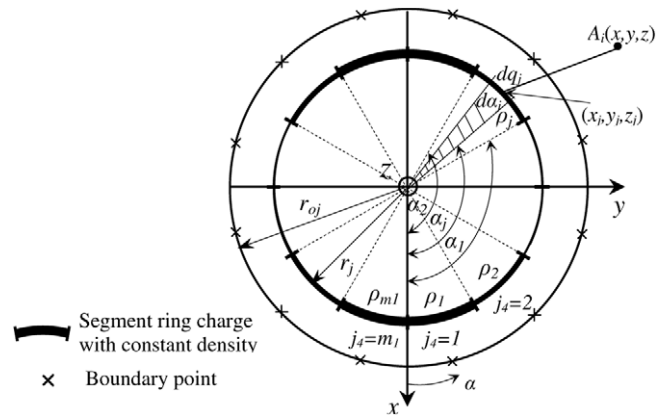

Figure 4. Discrete simulation ring charge, divided into equal segment ring charges with a constant charge density, placed at section A–A in figure 3.

Each line charge is divided into a definite number k of finite line charges, which is determined according to the accuracy level. Hence, the number of simulation charges for each cylinder is n times k charges.

The presence of particles in a co-axial cylinder results in a three-dimensional field problem with an asymmetrical field about the particle surface due to the asymmetrical influence of the co-axial cylinder on the particle surface electric field and the asymmetrical position of the particle inside the gap. The distributed charge on the surface of a spherical or a wire particle is replaced by two point charges and a set of m ring charges arranged inside it, figure 3. To account for the asymmetry created by the presence of particles, a new charge distribution is presented where the surface charges on the particles are simulated by fictitious ring charges with variable charge density along their entire perimeter. It can be assumed that the ring charge density remains constant within a certain angular range, figure 4. Hence, each ring charge is divided in

the simulation into a definite number of m_1 ring segments with constant charge density (ρ), which is determined according to the accuracy level.

For the spherical particle, the number of simulation charges inside the particle is $[2+(m \times m_1)]$; i.e. the total number of simulation charges is $N = [(2 \times n \times k) + 2 + (m \times m_1)]$.

The charge over the wire particle is simulated by two points, and m rings arranged inside the particle, figure 3. For the cylindrical part of the wire particle, the surface charge is simulated by uniformly distributed m_2 rings that vary in number depending on the wire shape factor (ℓ_w/r_w), which is defined as the wire cylindrical part length(ℓ_w) to its radius(r_w) ratio, m_2 equals an integer of $[f_1 \times (\ell_w/r_w)]$. For each hemispherical tip, the surface charge is simulated by a point charge placed at a distance ($f_2 \times r_w$) from the tip centre and two ring charges arranged uniformly inside each tip. Each ring is divided in the simulation into a definite number of m_1 ring segments with constant charge density (ρ), which is determined according to the accuracy level, figure 4. Hence, the total number of simulation charges inside the wire particle is $[2 + (m \times m_1)]$; $m = (4 + m_2)$; i.e. the total number of simulation charges is $N = [(2 \times n \times k) + 2 + (m \times m_1)]$.

3.2.2. Coordinates of simulating charges. Figure 3 shows a cross section of the co-axial gap with a wire particle placed in contact with the inner cylinder. Inside the inner cylinder, simulating n line charges of varying longitudinal charge density are arranged uniformly at a radius of ($f_3 \times r$). Outside the outer cylinder, simulating n line charges are also arranged uniformly at a radius of $R_o = R + (f_4 \times r)$.

For the spherical particle, the location of the two point charges is at a distance of $\pm(f_5 \times r_s)$ from the particle centre at the z-axis. The first ring charge (i.e. $j_3 = 1$) is placed at $z_1 = r + (f_6 \times r_s)$, while the other rings are arranged according to the relation $z_{j3} = [z_1 + f_7 \times (j_3 - 1) \times r_s]$, and as shown in figure 4, the radius of the ring charge is a fraction f_8 of the particle radius r_{oj} at the same z-level, $r_{j3} = (f_8 \times r_{oj})$.

For the wire particle, a point charge is placed at a distance of ($f_2 \times r_w$) from the tip centre of each hemispherical tip and two ring charges are arranged uniformly inside each tip. For the cylindrical part, the surface charge is simulated by uniformly distributed m_2 rings.

The problem is now reduced to the determination of the optimum values of integers n, k, m, m_1, m_2 and factors $f_1 - f_8$.

3.2.3. Coordinates of boundary points. To satisfy the boundary conditions, a boundary point, corresponding to each simulation charge, is chosen along the surface of the co-axial cylinders and around the particle surface, figures 3 and 4. Hence, the number of boundary points equals the number of simulation charges (N). The boundary points corresponding to the simulation finite line and segment ring charges were chosen midway along the line and the segment at the cylinders and particle surfaces, respectively. Also, for the simulation point charges, boundary points were chosen at the particle tip and at the touch points.

3.2.4. Potential calculation. The potential (φ_i) at an arbitrary boundary point $A_i(x, y, z)$ is linearly related to all simulation charges by

$$\phi_i = \sum_{j=1}^{j=N} p_{i,j} q_j, \tag{3}$$

where $p_{i,j}$ is the potential coefficient calculated at the ith boundary point due to the jth simulation charge q_j as expressed in appendix C.

3.2.5. Electric field calculation. It is well known that the electric field intensity (E) is the negative gradient of the potential φ. It is given, at an arbitrary point $A_i(x, y, z)$, by the vector sum of the individual components contributed by the known simulation charges (points, finite lines and ring segments).

Hence, the field intensity components Ex_i, Ey_i and Ez_i at point $A_i(x, y, z)$ are obtained as follows:

$$Ex_i = \sum_{j=1}^{j=N} fx_{i,j} q_j, \qquad Ey_i = \sum_{j=1}^{j=N} fy_{i,j} q_j \qquad \text{and}$$

$$Ez_i = \sum_{j=1}^{j=N} fz_{i,j} q_j, \tag{4}$$

where $fx_{i,j}$, $fy_{i,j}$ and $fz_{i,j}$ are the x-, y- and z- field coefficients calculated at point $A_i(x, y, z)$ due to the jth simulation charge, as expressed in appendix C. Then, the field intensity at that point is calculated by

$$E_i = \sqrt{Ex_i^2 + Ey_i^2 + Ez_i^2} \tag{5}$$

4. Results and discussions

To check the charge simulation accuracy, check points were chosen midway between the boundary points on the surfaces of the particle and the co-axial cylinders. The voltage deviation from the applied voltage and the field deviation from being normal to the surfaces of the particle and cylinders were assessed to check how well the boundary conditions are satisfied. This check of simulation accuracy was made for (i) a wide range of R to r ratios (1.5–500), (ii) r_s to r ratios (0.0001–0.25), (iii) r_w to r ratios (0.005–0.25), wire shape factors, i.e. the cylindrical part length ℓ_w to wire radius r_w ratio (0.2–78). The accuracy remained the same for these investigated ranges with a maximum percentage voltage error of 0.05% and a maximum field deviation angle of 2.5°. Malik [13] stated that potential error values less than 0.1% are considered reasonable for an accurate field solution.

The accuracy of a simulation depends strongly on the assumptions concerned with the choice of the number and the coordinates of the simulation charges. The optimum values of factors $f_1 - f_8$ are $f_1 = 2$, $f_2 = 0.5$, $f_3 = 0.1$, $f_4 = 5$, $f_5 = 0.015$, $f_6 = 0.12$, $f_7 = 0.045$ and $f_8 = 0.55$. The number of charges was found to be as follows: (i) for co-axial cylinders $n = 6$, $k = 100$, (ii) for spherical particle $m = 12$, $m_1 = 30$, (iii) for wire particle $m = 4 + m_2$, $m_2 = 1$–156 for (ℓ_w/r_w) = 1 to 78, $m_1 = 60$. Hence, the total

Table 1. Maximum values of per cent voltage error and field deviation angle at the spherical particle surface lying at the co-axial configuration ($r = 6$ mm, $R = 41$ mm).

Particle position	$r_s = 0.5$ mm		$r_s = 1.5$ mm	
	Inner cylinder	Outer cylinder	Inner cylinder	Outer cylinder
Max.% voltage error	5.5×10^{-4}%	5×10^{-4}%	6×10^{-3}%	4.5×10^{-3}%
Max. field deviation angle	$1.9°$	$0.3°$	$1.7°$	$1.6°$

Table 2. Maximum values of per cent voltage error and field deviation angle at the wire particle surface lying at the co-axial configuration ($r = 5.5$ mm, $R = 41$ mm).

Particle position	$r_w = 0.25$ mm, $\ell_w = 0.25$		$r_w = 0.25$ mm, $\ell_w = 20$	
	Inner cylinder	Outer cylinder	Inner cylinder	Outer cylinder
Max.% voltage error at the wire hemispherical tip	0.018%	2.5×10^{-3}%	0.025%	4×10^{-3}%
Max. field deviation angle at the wire hemisphere	$1.5°$	$1.5°$	$1.8°$	$1.5°$
Max.% voltage error at the wire cylindrical part	1.8×10^{-3}%	2×10^{-4}%	2×10^{-3}%	4×10^{-4}%
Max. field deviation angle at the wire cylindrical part	$1.5°$	$1.3°$	$2.5°$	$1.5°$

number of simulation charges (N) in the presence of spherical particles is 1562 and N in the presence of wire particles varies from 1502 to 10 802 for the two limits of the wire shape factor.

4.1. Simulation accuracy

The per cent voltage error and field deviation angle are calculated all over the surface of the spherical particle (α and θ start from $0°$ to $360°$ and $0°$ to $105°$, respectively, except for the narrow zone that lies near the touch point, as reported before in [12] over the stranded conductor surface). Table 1 presents the maximum values of per cent voltage error and field deviation angle for spherical particles of different radii ($r_s = 0.5$ mm, 1.5 mm) lying at the inner and outer cylinders of the co-axial configuration ($r = 6$ mm, $R = 41$ mm).

For wire particle, the per cent voltage error and field deviation angle are calculated all over the surface of the wire particle (hemispherical tip and cylindrical part). Table 2 presents the maximum values of per cent voltage error and field deviation angle for wire particles of different shape factors ($r_w/\ell_w = 1$ and $r_w/\ell_w = 20$) lying at the inner and outer cylinders of the co-axial configuration ($r = 5.5$ mm, $R = 41$ mm).

4.2. Comparison between present and previous calculations of the electric field distribution

The field in the investigated gap, in the presence of spherical particles, was calculated using CST [5]. Figure 5 shows a comparison between present and previous calculations of the electric field distribution in an optimized co-axial gap (where $\ln(R/r) \approx 1$) in the presence of a spherical particle at the outer cylinder. The comparison shows good agreement between the present and previous calculated field values. It is shown that the field in the gap is disturbed due to the presence of the particle
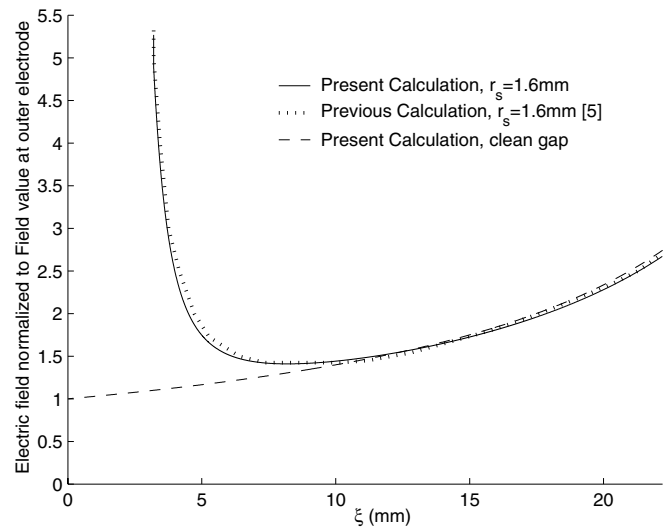

Figure 5. Electric field distribution in a co-axial cylinder in the presence of spherical particles ($r_s = 1.6$ mm) at the outer cylinder ($r = 12.7$ mm, $R = 34.9$ mm); the variable ξ starts from the surface of the outer cylinder.

up to a distance beyond the tip of the particle approximately double the particle diameter. Beyond that distance the field converges to the non-perturbed cylindrical field distribution.

4.3. Field intensification factor at the particle surface tip

In the presence of the particle, the electric field is distorted in the vicinity of its surface. The field pattern around the particle depends on the particle shape, size and position. For the presence of particle at the inner cylinder, the field intensification factor is the electric field strength at the particle tip divided by the field strength at the inner cylinder of the clean gap. The field intensification factor at the particle
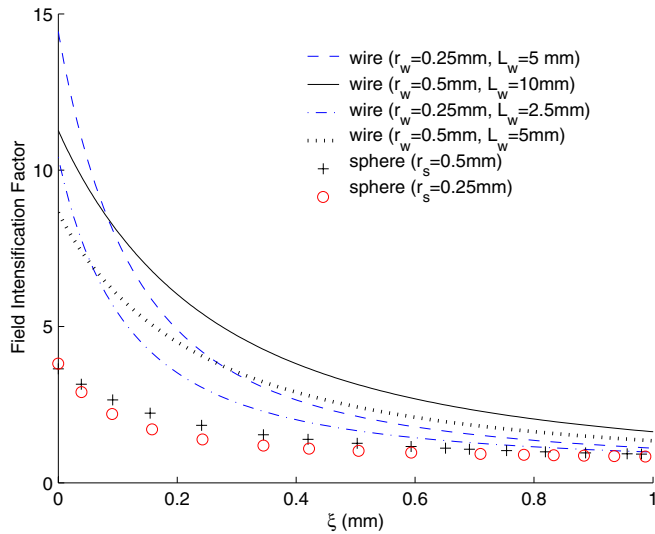
Figure 6. Field intensification factor of the wire and spherical particles lying at the inner cylinder ($r = 5.5\,\text{mm}$, $R = 41\,\text{mm}$).

Table 3. Corona onset voltage, field intensification factor and ionization-zone thickness for spherical particles of varying radii lying at the inner cylinder ($r = 5.5\,\text{mm}$, $R = 41\,\text{mm}$).

Spherical particle r_s (mm)	Field intensification factor	Ionization-zone thickness (mm)	Corona onset voltage (kV)
0.25	3.81	0.94	31.4
0.5	3.65	0.82	27

surface tip is responsible for the development of the corona discharge. When the criterion of self-sustained discharge is used to determine the onset voltage of the negative corona, the avalanche growth is computed in actual space, which depends on the spatial field distribution.

To demonstrate the effect of particle shape and size on the field intensification factor, figure 6 is plotted for two spheres of varying radii and wire particles of different shape factors lying at the inner cylinder, and the corresponding value of ionization-zone thickness and corona onset voltage are shown in tables 3 and 4, and the following results were obtained. (a) The spatial field distribution of the bigger spherical particle is higher than that of the smaller one; hence, the bigger particle will have a smaller onset voltage. (b) The ionization-zone thicknesses are approximately equal for the wire particles having the same radii and are independent of their lengths. (c) The onset voltages are approximately equal for the wire particles having the same shape factors; this is because the onset voltage depends on the growth of the primary avalanche, which depends mainly on the spatial field distribution. (d) The thinner one of wire particles having the same length and the longer one of wire particles having the same radius lead to the onset of a corona at lower applied voltages. (e) The onset voltage at wire particles is less than the onset voltage at spherical particles having the same radii; the presence of wire particle is more severe than the spherical one. These results agree well with those obtained in [6], where the wire particle was found free in a uniform field.

4.4. Comparison between calculated and measured onset voltages of the negative corona

Laboratory measurements of the onset voltage of a particle-initiated negative corona in the air-insulated co-axial configuration were carried out to check the accuracy of the present calculation. The calculated values were corrected to the ambient temperature and pressure, appendix B. The particles used are of different shapes and sizes.

4.4.1. Onset voltage of the negative corona of spherical particles. Figure 7 shows the calculated and measured onset voltage of the negative corona initiated by spherical particles lying at the inner cylinder of the air-insulated co-axial configuration. As shown in the figure, when the particle size increased, a slow reduction in the onset voltage is achieved for different inner cylinder radii, because the difference in the spatial field distribution is small (figure 6). The calculated values agreed satisfactorily with those measured experimentally with a deviation not exceeding 4.3%. The relative standard deviation of the mean value was generally smaller than 0.44%.

In the laboratory, using spherical particles of radii 1, 1.25, 1.5, 2 and 2.5 mm at the outer cylinder of the cylindrical configuration ($r = 23.5\,\text{mm}$ and $R = 41\,\text{mm}$), breakdown occurred without a proceeding corona.

4.4.2. Onset voltage of the negative corona of wire particles fixed radially at the inner cylinder. Figure 8 shows the calculated and measured onset voltage of the negative corona initiated by wire particles of different radii and shape factors, fixed radially at the inner cylinder of the co-axial configuration ($r = 5.5\,\text{mm}$ and $R = 41\,\text{mm}$). The calculated values agreed satisfactorily with those measured experimentally with a deviation not exceeding 7%. The relative standard deviation of the mean value was generally smaller than 0.25%. Figure 8 shows that the existence of wire particles at the inner cylinder leads to the onset of the corona at lower applied voltages for the cases of (a) thinner one of wires having the same length, (b) longer one of wires having the same radius, while the corona onset voltage is approximately equal for wires having the same shape factor.

4.4.3. Onset voltage of the negative corona of wire particles fixed radially at the outer cylinder. Figure 9 shows the calculated and measured onset voltage of the negative corona initiated by wire particles of different radii and shape factors, fixed radially at the outer cylinder of the co-axial configuration ($r = 5.5\,\text{mm}$ and $R = 41\,\text{mm}$). The calculated values agreed satisfactorily with those measured experimentally with a deviation not exceeding 4.4%. The relative standard deviation of the mean value was generally smaller than 0.26%. Also, figure 9 shows that the existence of wire particles at the outer cylinder leads to the onset of the corona at lower applied voltages for the cases of (a) thinner one of wires having the same length, (b) longer one of wires having the same radius, (c) longer one of wires having the same shape factor.

Table 4. Corona onset voltage, field intensification factor and ionization-zone thickness for wire particles of different shape factors lying at the inner cylinder ($r = 5.5$ mm, $R = 41$ mm).

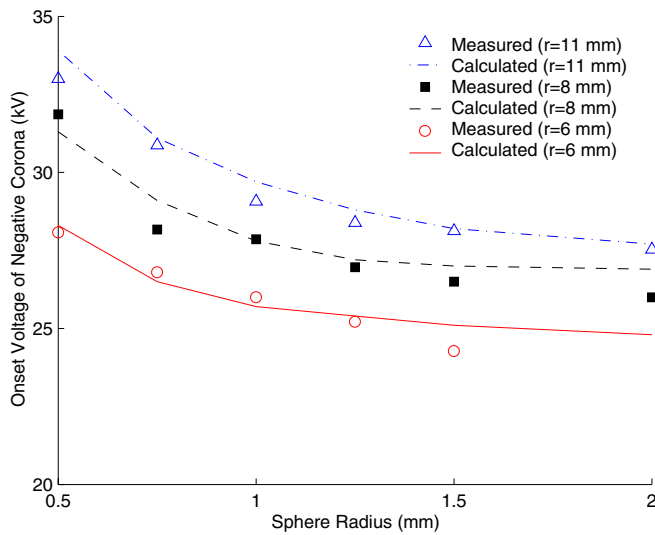| r_w (mm)	ℓ_w (mm)	ℓ_w/r_w	Field intensification factor	Ionization-zone thickness (mm)	Corona onset voltage (kV)
0.25	2.5	10	10.4	0.367	12.55
0.25	5	20	14.4	0.35	8.89
0.5	5	10	8.6	0.54	11.98
0.5	10	20	11.2	0.53	9

Figure 7. Measured and calculated onset voltage of a corona initiated by spherical particles, with varying radii, lying at the inner cylinder of different co-axial configurations, ($R = 41$ mm).
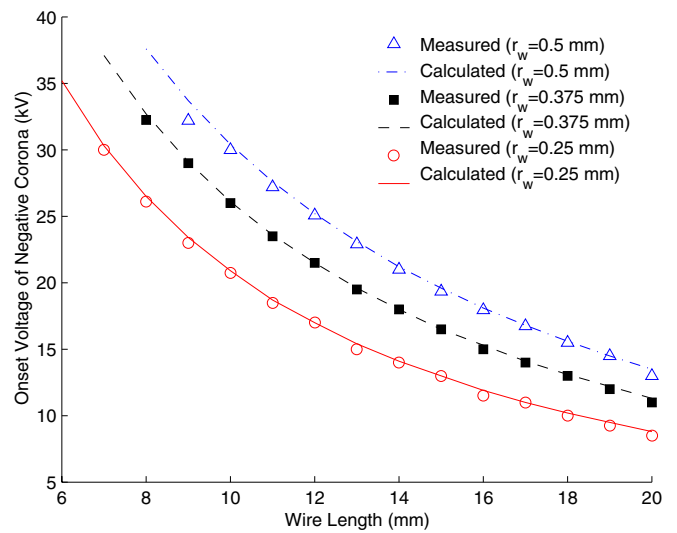

Figure 9. Measured and calculated corona onset voltage initiated by wire particles of different shape factors, fixed radially at the outer cylinder of co-axial configuration ($r = 5.5$ mm, $R = 41$ mm).
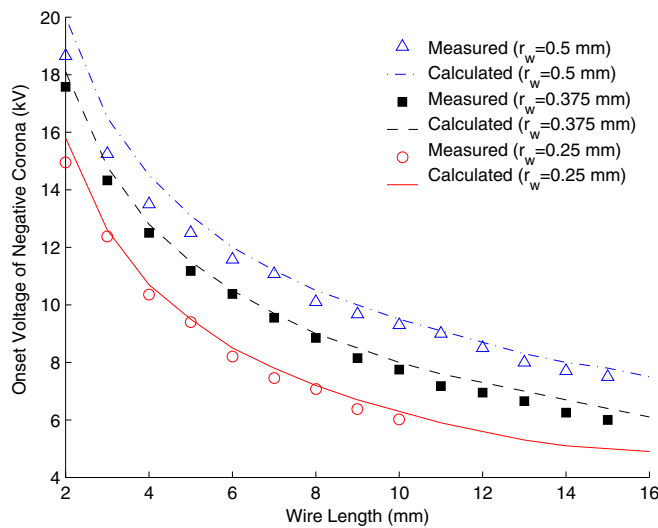
4.5. Onset voltage of the negative corona initiated by particles in the air-insulated co-axial configuration

Figure 10 shows the calculated onset voltage of the corona in a clean gap and in the presence of spherical and wire particles of different radii and shape factor, lying at the inner cylinder of the pressurized air-insulated co-axial cylinder ($r = 5.5$ mm and $R = 41$ mm). This figure shows that the corona onset voltage is decreased substantially in the presence of particles, and the wire particle is more harmful than the spherical one and their effects are more pronounced at higher gas pressures.

In figure 10, below 6 atmospheric air pressure only photoemission is considered to be the active secondary mechanism responsible for supplying secondary electrons [7, 15], where the field strength is less than 5×10^7 V m^{-1}, while above 6 atmospheric air pressure, the field strength exceeds 5×10^7 V m^{-1}, and photoemission and field emission from the cathode surface are considered to be active secondary mechanisms.

Figure 8. Measured and calculated corona onset voltage initiated by wire particles of different shape factors fixed radially at the inner cylinder of co-axial configuration ($r = 5.5$ mm, $R = 41$ mm).

Figures 8 and 9 show that the corona onset voltage in the presence of wire particles at the inner cylinder is less than that, of the same dimension, at the outer cylinder, i.e. the presence of wire particles at the inner cylinder is more severe than their presence at the outer cylinder.

5. Conclusions

(1) The three-dimensional electric field is accurately calculated in a co-axial configuration in the presence of spherical or wire particles, fixed at the inner or the outer cylinder, using CST with a new charge distribution due to the asymmetrical field about the particle surface.
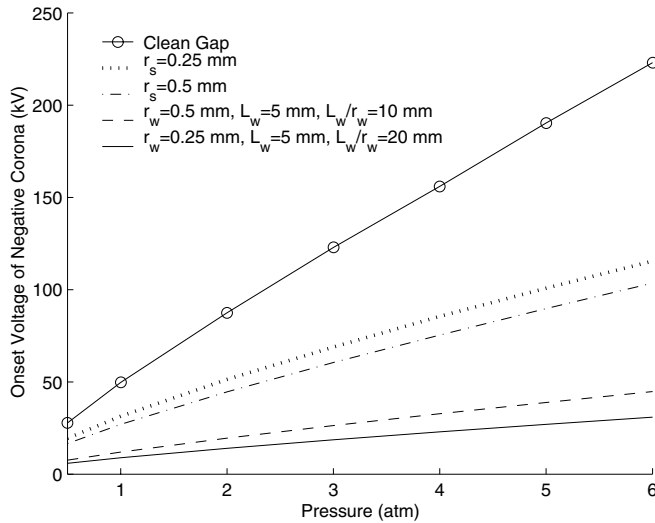
J. Phys. D: Appl. Phys. **46** (2013) 045205

M M El Bahy *et al*

Figure 10. Calculated corona onset voltage initiated from spherical or wire particles, lying at the inner cylinder ($r = 5.5$ mm, $R = 41$ mm).

(2) In the presented charge distribution, the surface charges on the particle are simulated by point charges and fictitious ring charges with variable charge density along their entire perimeter, and each ring charge is divided into a definite number of ring segments with constant charge density assuming that the ring charge density remains constant within a certain angular range.

(3) The presence of particles significantly reduces the corona onset voltage and dielectric strength of the co-axial configuration, and the presence of particles at the inner cylinder is more severe than their presence on the outer one also, and the wire particle is more severe than the spherical one.

(4) The ionization-zone thicknesses were approximately equal for the wire particles having the same radii and independent of their lengths.

(5) For wire particles lying at the inner or the outer cylinder, increasing wire length of the same radius (longer one) or decreasing wire radius of the same length (thinner one) leads to the onset of corona at lower applied voltages.

(6) The corona onset voltage of wire particles, lying at the inner cylinder, having the same shape factor is approximately equal, while the corona onset voltage of wire particles, lying at the outer cylinder, having the same shape factor is decreased with increasing wire length.

(7) The spatial field distribution of the bigger spherical particle is higher than that of the smaller one; hence, the bigger particle will have a smaller onset voltage.

(8) The calculated onset voltage and dielectric strength decrease substantially in the presence of particles in the pressurized air-insulated co-axial configuration and the wire particles are more harmful and their effects are more pronounced at higher gas pressures.

(9) The calculated corona onset voltage values agreed satisfactorily with those measured experimentally with a deviation not exceeding 7%.
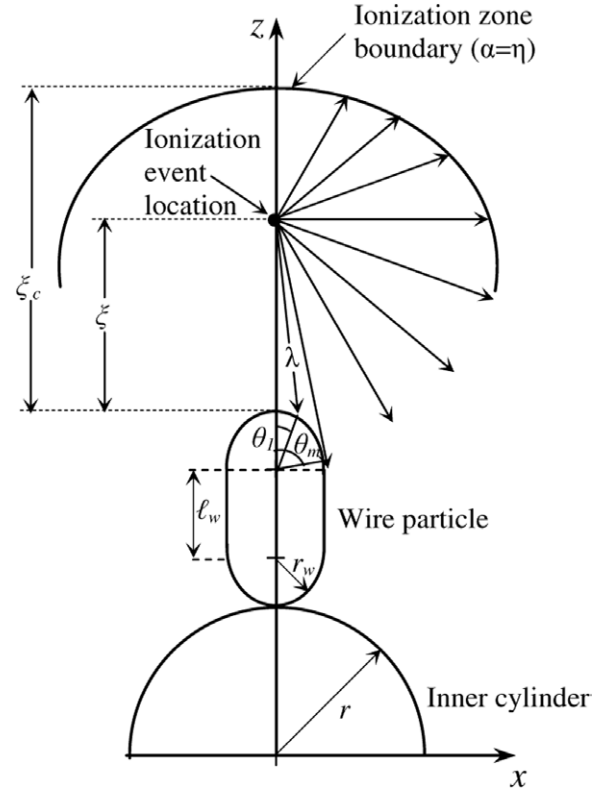

Figure A1. Propagation of photon in the ionization zone in radial directions from an ionization event along the route of the avalanche.

Appendix A. Calculation of geometry factor $g(\xi)$

The geometry factor is given in [12] in terms of its radial component $g_{rad}(\xi)$ times axial components $g_{axial}(\xi)$, and as shown in figure A1, $g_{rad}(\xi) = g_{axial}(\xi)$ the geometry factor is as follows:

$$g_{rad}(\xi) = \frac{1}{\pi e^{-\mu\xi}} \int_0^{\theta_m} e^{-\mu\sqrt{\lambda}} \, d\theta_1$$

$$\lambda = (r_s + \xi)^2 + r_s^2 - 2r_s(r_s + \xi) \cos\theta_1$$

$$\theta_m = \cos^{-1}\left[\frac{r_s}{r_s + \xi}\right]$$

$$g(\xi) = g_{rad}(\xi) \times g_{rad}(\xi).$$

Appendix B. Discharge parameters

Ionization and attachment coefficients in air are as follows [17]:

$$\frac{\alpha}{\delta}(\text{cm}^{-1}) = 3632 e^{\left(-168\frac{\delta}{E}\right)}$$

$$\text{for } 19 < \frac{E}{\delta} < 45.6 \, \text{kV cm}^{-1}$$

$$\frac{\alpha}{\delta}(\text{cm}^{-1}) = 7358 e^{\left(-200.6\frac{\delta}{E}\right)}$$

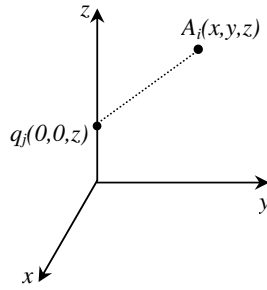$$\text{for } 45.6 < \frac{E}{\delta} < 182.4 \, \text{kV cm}^{-1}$$

Figure C1. Point charge q_j lying along the z-axis.

$$\frac{\alpha}{\delta}(\text{cm}^{-1}) = 11\,424.8\mathrm{e}^{\left(-277\frac{\delta}{E}\right)}$$

$$\text{for } 182.4 < \frac{E}{\delta} < 608\,\text{kV cm}^{-1}$$

$$\frac{\eta}{\delta}(\text{cm}^{-1}) = 9.8648 - 0.541\left(\frac{E}{\delta}\right) + 0.011\,4474\left(\frac{E}{\delta}\right)^2$$

$$\delta = \frac{(293) \times P}{760 \times (273 + T)},$$

where E is the electric field in kV cm^{-1}, δ is the relative air density factor, P is the air pressure in Torr and T is the air temperature in °C. The photon absorption coefficient in air [7]

$$\mu = \mu_0 P \qquad \text{at } P \leqslant 760\,\text{Torr}$$

$$\mu = \mu_0 \qquad \text{at } P > 760\,\text{Torr},$$

where μ_0 is the absorption coefficient at atmospheric pressure, $\mu_0 = 500\,\text{m}^{-1}$ in air [7]. Townsend's second coefficient γ_{ph} due to the action of photons is constant at its value, 0.003 for air [7].

Appendix C. Potential and field coefficients

C.1. Point charge along the z-axis

For a point charge q_j located at the coordinates $(0,0,z_j)$, figure C1, the potential coefficient at the ith space point $A_i(x, y, z)$ is expressed as

$$p_{i,j} = \frac{1}{4\pi\varepsilon_0\sqrt{x^2 + y^2 + (z - z_j)^2}}, \qquad \text{(C.1.1)}$$

where ε_0 is the permittivity of free space. The field coefficients at the ith space point $A_i(x, y, z)$ are expressed as

$$fx_{i,j} = \frac{x}{4\pi\varepsilon_0(\sqrt{x^2 + y^2 + (z - z_j)^2})^3} \qquad \text{(C.1.2)}$$

$$fy_{i,j} = \frac{y}{4\pi\varepsilon_0(\sqrt{x^2 + y^2 + (z - z_j)^2})^3} \qquad \text{(C.1.3)}$$

$$fz_{i,j} = \frac{(z - z_j)}{4\pi\varepsilon_0(\sqrt{x^2 + y^2 + (z - z_j)^2})^3}. \qquad \text{(C.1.4)}$$
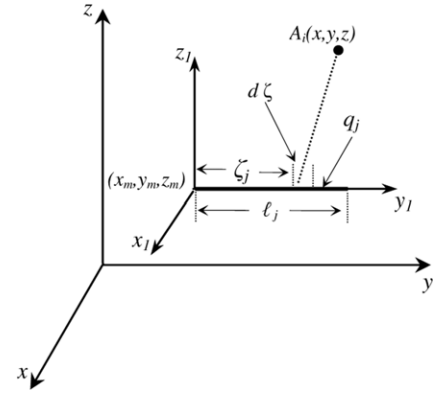

Figure C2. Finite line charge (q_j) assigned to new coordinates (x_1, y_1, z_1).

C.2. Finite line charge parallel to the y-axis

A finite line charge q_j extending parallel to the y-axis starts at coordinates (x_m, y_m, z_m) and has a length of ℓ_j, figure C2. Each infinitesimal length $\mathrm{d}\zeta$ of the main charge (q_j) is assumed to be a point charge distant $\sqrt{(x_1)^2 + (\zeta_j - y_1)^2 + (z_1)^2}$ from the space point $A_i(x_1, y_1, z_1)$; $x_1 = x - x_m$, $y_1 = y - y_m$, $z_1 = z - z_m$.

The infinitesimal length $\mathrm{d}\zeta$ has an infinitesimal charge $\mathrm{d}q_j$,

$$\mathrm{d}q_j = \frac{q_j}{\ell_j}\,\mathrm{d}\zeta.$$

Then, the potential at point $A_i(x_1, y_1, z_1)$ due to this infinitesimal charge $(\mathrm{d}q_j)$ is

$$\mathrm{d}\phi_i = \frac{\mathrm{d}q_j}{4\pi\varepsilon\sqrt{(x_1)^2 + (\zeta_j - y_1)^2 + (z_1)^2}}$$

$$\mathrm{d}\phi_i = \frac{q_j}{4\pi\varepsilon\ell_j\sqrt{(x_1)^2 + (\zeta_j - y_1)^2 + (z_1)^2}}\,\mathrm{d}\zeta.$$

Then, the potential coefficient for the infinitesimal length is

$$\mathrm{d}p_{i,j} = \frac{1}{4\pi\varepsilon\ell_j\sqrt{(x_1)^2 + (\zeta_j - y_1)^2 + (z_1)^2}}\,\mathrm{d}\zeta.$$

Integrating along the length ℓ_j of the finite line charge (q_j), the potential coefficient will be

$$p_{i,j} = \frac{1}{4\pi\varepsilon_0\ell_j}\left[\ln\frac{(\ell_j - y_1) + \gamma}{(-y_1) + \delta}\right] \qquad \text{(C.2.1)}$$

$$\gamma = \sqrt{(x_1)^2 + (\ell_j - y_1)^2 + (z_1)^2}$$

$$\delta = \sqrt{(x_1)^2 + (y_1)^2 + (z_1)^2}.$$

The field coefficients at the ith space point are expressed as

$$fx_{i,j} = \frac{1}{4\pi\varepsilon_0\ell_j}\left[\frac{x_1}{(x_1)^2 + (z_1)^2}\right]\left[\frac{(\ell_j - y_1)}{\gamma} + \frac{y_1}{\delta}\right] \quad \text{(C.2.2)}$$

$$fy_{i,j} = \frac{1}{4\pi\varepsilon_0\ell_j}\left[\frac{1}{\gamma} - \frac{1}{\delta}\right] \qquad \text{(C.2.3)}$$

$$fz_{i,j} = \frac{1}{4\pi\varepsilon_0\ell_j}\left[\frac{z_1}{(x_1)^2 + (z_1)^2}\right]\left[\frac{(\ell_j - y_1)}{\gamma} + \frac{y_1}{\delta}\right]. \quad \text{(C.2.4)}$$

J. Phys. D: Appl. Phys. **46** (2013) 045205

M M El Bahy *et al*

C.3. Segment ring charge with constant charge density (ρ_j)

In figure 3, the ring charge is divided into a number of segment ring charges. Let q_j be the total charge on the segment ring charge (j), then the charge density of this segment ring charge (ρ_j) is

$$\rho_j = \frac{q_j}{(\alpha_2 - \alpha_1)r_j}.$$

For an infinitesimal segment ring charge ($\mathrm{d}q_j$),

$$\mathrm{d}q_j = \rho_j \cdot r_j \cdot \mathrm{d}\alpha_j$$

$$\mathrm{d}q_j = \frac{q_j}{(\alpha_2 - \alpha_1)}\mathrm{d}\alpha_j,$$

Assuming that each infinitesimal segment ring charge ($\mathrm{d}q_j$) is a point charge, then the potential $\mathrm{d}\phi_i$ at point $A_i(x, y, z)$ due to the point charge ($\mathrm{d}q_j$) is

$$\mathrm{d}\phi_i = \frac{1}{4\pi\varepsilon\sqrt{(x_j - x)^2 + (y_j - y)^2 + (z_j - z)^2}}\,\mathrm{d}q_j$$

$$\mathrm{d}\phi_i = \frac{q_j}{4\pi\varepsilon(\alpha_2 - \alpha_1)\sqrt{(x_j - x)^2 + (y_j - y)^2 + (z_j - z)^2}}\,\mathrm{d}\alpha_j$$

$$\mathrm{d}\phi_i = \mathrm{d}p_{i,j}.q_j.$$

Hence,

$$\mathrm{d}p_{i,j}$$
$$= \frac{1}{4\pi\varepsilon(\alpha_2 - \alpha_1)\sqrt{(x_j - x)^2 + (y_j - y)^2 + (z_j - z)^2}}\,\mathrm{d}\alpha_j.$$

Integrating along the arc charge q_j, the potential coefficient will be

$$p_{i,j} = \frac{1}{4\pi\varepsilon(\alpha_2 - \alpha_1)}$$
$$\times \int_{\alpha_1}^{\alpha_2} \frac{1}{\sqrt{(x_j - x)^2 + (y_j - y)^2 + (z_j - z)^2}}\,\mathrm{d}\alpha_j$$

$$p_{i,j} = \frac{1}{4\pi\varepsilon(\alpha_2 - \alpha_1)}$$
$$\times \int_{\alpha_1}^{\alpha_2} [1]\big[[x^2 + y^2 + r_j^2 - 2xr_j\cos\alpha_j$$
$$-2yr_j\sin\alpha_j + (z_j - z)^2]^{\frac{1}{2}}\big]^{-1}\,\mathrm{d}\alpha_j, \tag{C.3.1}$$

where $r_j = \sqrt{x_j^2 + y_j^2}$.

The field coefficients at the ith space point are expressed as

$$fx_{i,j} = \frac{1}{4\pi\varepsilon(\alpha_2 - \alpha_1)}\int_{\alpha_1}^{\alpha_2}[(x - r_j\cos\alpha_j)]$$
$$\times \big[[x^2 + y^2 + r_j^2 - 2xr_j\cos\alpha_j - 2yr_j\sin\alpha_j$$
$$+ (z_j - z)^2]^{\frac{3}{2}}\big]^{-1}\,\mathrm{d}\alpha_j \tag{C.3.2}$$

$$fy_{i,j} = \frac{1}{4\pi\varepsilon(\alpha_2 - \alpha_1)}\int_{\alpha_1}^{\alpha_2}[(y - r_j\sin\alpha_j)]$$
$$\times \big[[x^2 + y^2 + r_j^2 - 2xr_j\cos\alpha_j - 2yr_j\sin\alpha_j$$
$$+ (z_j - z)^2]^{\frac{3}{2}}\big]^{-1}\,\mathrm{d}\alpha_j \tag{C.3.3}$$

$$fz_{i,j} = \frac{1}{4\pi\varepsilon(\alpha_2 - \alpha_1)}\int_{\alpha_1}^{\alpha_2}[(z_j - z)]$$
$$\times \big[[x^2 + y^2 + r_j^2 - 2xr_j\cos\alpha_j$$
$$- 2yr_j\sin\alpha_j + (z_j - z)^2]^{\frac{3}{2}}\big]^{-1}\,\mathrm{d}\alpha_j. \tag{C.3.4}$$

References

[1] Cigre working group D1-11 2003 Knowledge rules of partial discharge diagnosis in service *Electra* **207** 63–6

[2] Metwally I A and Rahim A A A 2002 Factors affecting the dynamics of wire particles in gas insulated systems *Eur. Trans. Electr. Power* **11** 403–12

[3] Sarathi R and Umamaheswari R 2009 Understanding the partial discharge activity initiated by a conducting particle in GIS under DC voltages using UHF technique *J. Electr. Eng.* **60** 136–42

[4] Cooke C M 1975 Ionization, electrode surface and discharge in SF$_6$ at extra-high voltages *IEEE Trans. Power Apparatus Syst.* **94** 1518–23

[5] Rizk F A M, Masetti C and Comsa R P 1979 Particle-initiated breakdown in SF$_6$ insulated systems under high direct voltag *IEEE Trans. Power Apparatus Syst.* **98** 825–36

[6] Anis H and Srivastava K D 1981 Free conducting particles in compressed gas insulation *IEEE Trans. Electr. Insul.* **16** 327–38

[7] Abdel-Salam M, Ahmed A and Nasr EL-Deen A 2010 Inception voltage of corona discharge from suspended, grounded and stressed particles in uniform-field gas-insulated-gaps at varying pressures *Int. J. Plasma Environ. Sci. Technol.* **4** 1–12

[8] I Metwally A and Rahim A A A 2002 Dynamic analysis of spherical metallic particles in non-uniform electric field *IEEE Trans. Dielectr. Electr. Insul.* **9** 282–93

[9] Sahu K B M and Amarnath J 2010 Effect of various parameters on the movement of metallic particles in a single phase gas insulated bus duct with image charges and dielectric coated electrodes *ARPN J. Eng. Appl. Sci.* **5** 52–6

[10] Subrahmanyam K B V S R and Amarnath J 2011 Image charge effect on metallic particle in single phase gas insulated bus duct (GIB) *J. Emerging Trends Eng. Appl. Sci., (JETEAS)* **2** 451–5

[11] Asano K, Yatsuzuka K and Yamaki T 2000 DC Corona discharge of a metal filament particle within parallel-plate electrodes *IEEE Trans. Industry Appl.* **36** 87–92

[12] El-Bahy M M, Abouelsaad M, Abdel-Gawad N and Badawi M 2007 Onset voltage of negative corona on stranded conductors *J. Phys. D: Appl. Phys.* **40** 3094–101

[13] Malik N H 1989 A review of the charge simulation method and its applications *IEEE Trans. Electr. Insul.* **24** 3–14

[14] Utmischi D 1979 Charge substitution method for three-dimensional high voltage fields *3rd Int. Symp. High Voltage Engineering (Milan, Italy)*

[15] Abdel-Salam M 1987 Discharge inception in high-voltage three-electrode systems *J. Phys. D: Appl. Phys.* **20** 629–34

[16] Parekh H and Srivastava K D 1979 Effect of avalanche space charge field on the calculation of corona onset voltage *IEEE Trans. Electr. Insul.* **EI-14** 181–92

[17] Tiebing Lu, Gaolin Xiong, Xiang Gui, Hong Rao and Qi Wang 2011 Analysis of corona onset electric field considering the effect of space charges *IEEE Trans. Mag.* **47** 1390–93